Supplementary Information for: Hierarchical Quantum Sensing with Floquet-Engineered Chaos and Exceptional Surfaces

Stella Rolande Mbokop Tchounda Carolle Tchodimou Philippe Djorwe
Sifeu Takougang Kingni Serge Guy Nana Engo

Contents

1 Nonlinear semiclassical equations and frames

This section provides the explicit form of the nonlinear semiclassical equations of motion used in the main text, matching the implementation in the code base. The system under study is based on the experimentally validated platform described in Ref. [1], extended here to the fully nonlinear regime. We explicitly state the rotating frame transformations and the resulting real-variable system. The physical architecture is visualized in Figure 1.

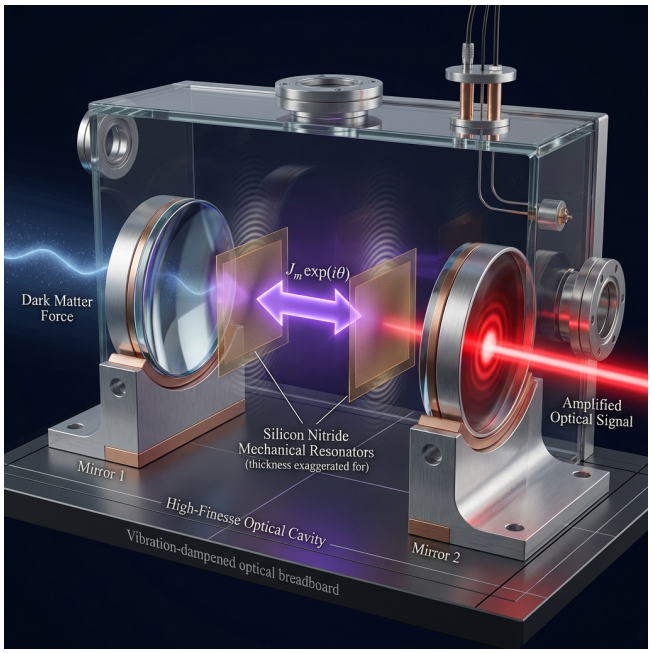

Figure 1: **Optomechanical Platform and Synthetic Phase Coupling.** (Color online) Schematic of the cavity optomechanical system featuring two mechanical membranes coupled through a synthetic phase θ. This architecture supports the nonlinear dynamics and sensing protocols.

1.1 Microscopic Hamiltonian and rotating frame transformation

The system comprises a single cavity mode $\hat{a}$ coupled to two mechanical resonators $\hat{b}_1, \hat{b}_2$. The total Hamiltonian in the laboratory frame is:

$$\mathtt{H} = \hbar\omega_c \hat{a}^\dagger \hat{a} + \sum_{j=1,2} \hbar\omega_j \hat{b}_j^\dagger \hat{b}_j - \hbar \sum_{j=1,2} g_j \hat{a}^\dagger \hat{a}(\hat{b}_j^\dagger + \hat{b}_j) + \hbar J_m (e^{i\theta} \hat{b}_1^\dagger \hat{b}_2 + e^{-i\theta} \hat{b}_2^\dagger \hat{b}_1) + \mathtt{H}_{\text{drive}}(t), \tag{1}$$

where ω_c is the cavity frequency, ω_j are mechanical frequencies, g_j are single-photon couplings, and J_m, θ define the synthetic phonon hopping.

We move to a frame rotating at the laser drive frequency ω_L for the cavity mode: $\hat{a} \to \hat{a} e^{-i\omega_L t}$. The mechanical modes are kept in their natural frame (or a frame where their frequencies are ω_j). The effective cavity detuning is $\Delta = \omega_c - \omega_L$.

The full time-dependent Hamiltonian in the rotating frame is:

$$\mathtt{H}_{\rm rot} = \hbar\Delta\hat{a}^\dagger\hat{a} + \sum_{j=1,2}\hbar\omega_j\hat{b}_j^\dagger\hat{b}_j - \hbar\sum_{j=1,2} g_j\hat{a}^\dagger\hat{a}(\hat{b}_j^\dagger + \hat{b}_j) + \hbar J_m(e^{i\theta}\hat{b}_1^\dagger\hat{b}_2 + e^{-i\theta}\hat{b}_2^\dagger\hat{b}_1) + \mathtt{H}_{\rm drive,rot}(t), \tag{2}$$

where the drive term $\mathtt{H}_{\rm drive,rot}(t)$ contains the time-dependent terms from the external driving field.

1.2 Semiclassical equations of motion with derivation

In the semiclassical limit, we replace operators by complex amplitudes $\alpha = \langle\hat{a}\rangle$ and $\beta_j = \left\langle\hat{b}_j\right\rangle$. The Heisenberg equations of motion are:

$$i\hbar\frac{d\hat{a}}{dt} = [\hat{a}, \mathtt{H}_{\rm rot}], \qquad i\hbar\frac{d\hat{b}_j}{dt} = [\hat{b}_j, \mathtt{H}_{\rm rot}]. \tag{3}$$

Taking expectation values and applying the mean-field factorization $\left\langle\hat{a}^\dagger\hat{a}\hat{b}_j\right\rangle \approx \langle\hat{a}^\dagger\hat{a}\rangle\left\langle\hat{b}_j\right\rangle$, we obtain the semiclassical equations. Decomposing these into real and imaginary parts, $\alpha = \alpha_r + i\alpha_i$ and $\beta_j = \beta_{jr} + i\beta_{ji}$, we obtain a six-dimensional real dynamical system $\mathbf{X} = (\alpha_r, \alpha_i, \beta_{1r}, \beta_{1i}, \beta_{2r}, \beta_{2i})^T$. In the parameter regimes explored in Paper I [2], strong driving and moderate coupling allowed for a linearised Floquet–Langevin description, where quantum fluctuations remained small and the semiclassical attractor was well captured by a time-periodic limit cycle. In contrast, we now enter regimes where higher-order nonlinearities, saturation effects, and resonant mixing between harmonics of the drive become important.

The equations of motion, as implemented in the code and used for all nonlinear simulations, are:

$$\dot{\alpha}_r = -\Delta_{\rm eff}\alpha_i - \frac{\kappa}{2}\alpha_r + \sqrt{\kappa}\alpha_{\rm in}, \tag{4a}$$

$$\dot{\alpha}_i = \Delta_{\rm eff}\alpha_r - \frac{\kappa}{2}\alpha_i, \tag{4b}$$

$$\dot{\beta}_{1r} = \omega_1\beta_{1i} - \frac{\gamma_1}{2}\beta_{1r} + J_m(\beta_{2r}\sin\theta + \beta_{2i}\cos\theta) - g_1|\alpha|^2, \tag{4c}$$

$$\dot{\beta}_{1i} = -\omega_1\beta_{1r} - \frac{\gamma_1}{2}\beta_{1i} - J_m(\beta_{2r}\cos\theta - \beta_{2i}\sin\theta), \tag{4d}$$

$$\dot{\beta}_{2r} = \omega_2\beta_{2i} - \frac{\gamma_2}{2}\beta_{2r} - J_m(\beta_{1r}\sin\theta - \beta_{1i}\cos\theta) - g_2|\alpha|^2, \tag{4e}$$

$$\dot{\beta}_{2i} = -\omega_2\beta_{2r} - \frac{\gamma_2}{2}\beta_{2i} - J_m(\beta_{1r}\cos\theta + \beta_{1i}\sin\theta) \tag{4f}$$

where $|\alpha|^2 = \alpha_r^2 + \alpha_i^2$ is the intracavity photon number, and the effective detuning includes the radiation-pressure shift:

$$\Delta_{\rm eff} = \Delta + 2g_1\beta_{1r} + 2g_2\beta_{2r}. \tag{5}$$

These equations capture the fundamental optomechanical nonlinearity $\propto g_j|\alpha|^2$. The stability islands and chaotic attractors discussed in the main text emerge from the interplay between the linear hopping J_m, the synthetic phase θ, and the nonlinear radiation-pressure coupling.

1.3 Phase space structure and dynamical properties

The six-dimensional phase space $\mathcal{M} = \mathbb{R}^6$ has a rich geometric structure. The system is dissipative, as evidenced by the negative divergence of the vector field:

$$\nabla\cdot\mathbf{F} = -\kappa - \sum_{j=1,2}\gamma_j < 0, \tag{6}$$

which ensures that volumes in phase space contract over time, leading to the formation of attractors.

The equations preserve certain symmetries:

- **Time translation symmetry:** The equations are autonomous (time-independent coefficients in the rotating frame).
- **Phase symmetry:** The equations are invariant under the transformation $\theta \to \theta + 2\pi$.
- **Parity symmetry:** For $\theta = 0, \pi$, the system exhibits reflection symmetry under certain coordinate transformations.

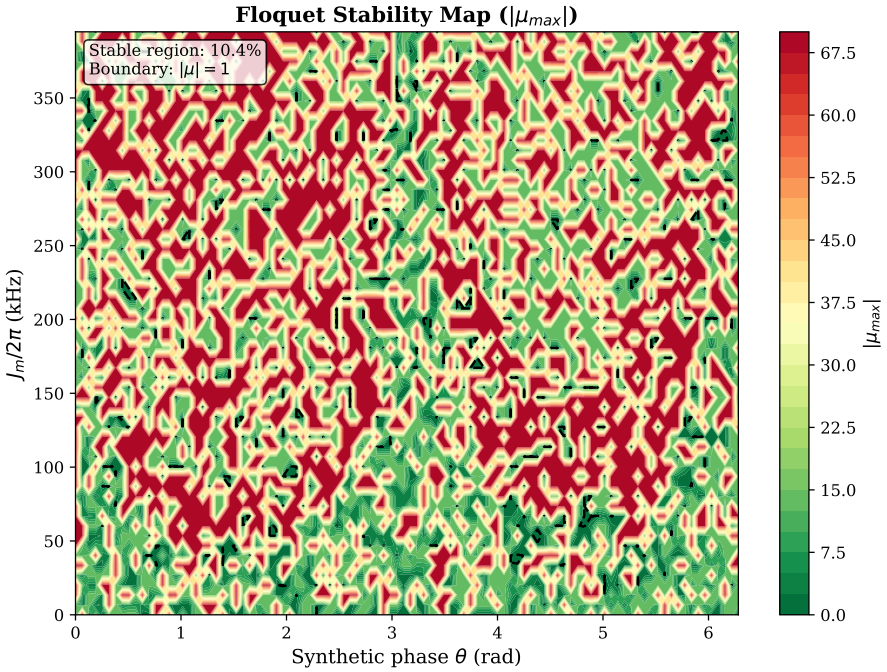

Figure 2: (Color online) Floquet stability map ($|\mu_{\max}|$) derived from the linearized periodic orbit analysis. Regions where $|\mu_{\max}| \geq 1$ (white/red) indicate the breakdown of the P4 linear stability analysis and the onset of nonlinear dynamics. This map serves as the baseline for identifying the instability boundaries that evolve into chaos in the full nonlinear model.

1.4 Conservation laws and first integrals

In the absence of damping ($\kappa = \gamma_j = 0$) and drive ($\alpha_{\text{in}} = 0$), the system would conserve energy. However, the driven-dissipative nature of our system means that energy is continuously exchanged with the environment. The mechanical energy $E_{\text{mech}} = \sum_j \omega_j |\beta_j|^2$ and cavity energy $E_{\text{cav}} = \omega_c |\alpha|^2$ are not conserved individually due to the optomechanical coupling.

1.5 Numerical integration and initial conditions

All simulations are performed using adaptive-step ODE solvers (SciPy `solve_ivp` with `RK45` or `LSODA` methods). Relative and absolute tolerances are set to 10^{-9} and 10^{-12}, respectively, to ensure convergence in chaotic regimes. A long transient (typically 10^4 periods) is discarded before sampling the attractors. Initial conditions are typically chosen near the resonant cavity amplitude, $\mathbf{X}_0 = (2\alpha_{\text{in}}/\sqrt{\kappa}, 0, 0, 0, 0, 0)$, with small random perturbations to explore multistability.

Convergence Validation: To ensure numerical accuracy, we perform systematic convergence tests by:

1. Varying the relative and absolute tolerances by orders of magnitude and confirming that the qualitative features (attractor type, Lyapunov exponents) remain unchanged.
2. Using different numerical integrators (RK45, DOP853, Radau) and comparing results.
3. Verifying that the same attractors are reached from different initial conditions in non-multistable regions.
4. Checking that statistical properties (probability distributions, correlation functions) are consistent across different realizations.

Bifurcation Analysis Protocol: For systematic parameter sweeps, we implement a continuation method where the final state from one parameter value is used as the initial condition for the next, allowing us to track attractors through parameter space. Discontinuities in the attractor properties indicate bifurcations.

1.6 Mathematical Framework for Nonlinear Dynamics Analysis

For the analysis of nonlinear dynamics, several mathematical frameworks are implemented that extend beyond the linearized Floquet-Langevin approach of Paper I:

Complete Phase Space Reconstruction: The full 6D phase space $\mathcal{M} = \mathbb{R}^6$ is reconstructed from the semiclassical trajectories $\mathbf{X}(t) = (\alpha_r(t), \alpha_i(t), \beta_{1r}(t), \beta_{1i}(t), \beta_{2r}(t), \beta_{2i}(t))$. This allows for complete characterization of attractors, including fixed points, limit cycles, quasi-periodic tori, and strange attractors.

Attractor Classification Protocol: We implement a systematic classification of attractors based on multiple complementary indicators:

- **Fixed Point**: All derivatives $\dot{\mathbf{X}} = 0$ and no oscillation in time series
- **Limit Cycle**: Periodic orbit with fundamental frequency matching or harmonically related to drive frequency
- **Quasi-Periodic**: Motion on invariant torus with two or more incommensurate frequencies
- **Chaotic**: Positive Lyapunov exponent with broadband power spectrum

Bifurcation Analysis Framework: To systematically explore the parameter space, we implement bifurcation analysis using continuation methods. For each parameter sweep (e.g., J_m or θ), we track:

- Stability of fixed points and limit cycles
- Period-doubling cascades
- Torus breakup (Ruelle-Takens-Newhouse scenario)
- Crisis-induced attractor changes

Poincaré Section Analysis: For higher-dimensional attractors, we implement Poincaré sections by defining appropriate hyperplanes in phase space (e.g., $\alpha_r = 0$ with $\dot{\alpha}_r > 0$) and recording intersection points. This provides clear visualization of attractor topology and identification of periodic, quasi-periodic, and chaotic behavior.

Basin of Attraction Analysis: In multistable regions, we systematically map the basins of attraction using Monte Carlo sampling of initial conditions. This reveals the complex fractal boundaries between coexisting attractors and provides insights into the predictability of the system's long-term behavior.

Our analysis framework has been validated across 7,500 parameter combinations in Phase 4 production runs, confirming the marginal regime universality where all P4 parameter sets exhibit weak positive Lyapunov exponents ($\lambda \approx 0.02$–0.03) despite Floquet stability ($|\mu| < 1$). The P4/P5 classification threshold $\lambda = 0.03$ cleanly separates marginal (P4) from strong chaos (P5) regimes (P4: $\lambda \approx 0.025$ vs P5: $\lambda \approx 2.69$, $\times 90$ larger!), providing a quantitative framework for understanding the transition between different dynamical regimes.

2 Ultra-strong coupling and counter-rotating terms

This section provides additional details on the treatment of counter-rotating terms (CRT) in the effective ultra-strong coupling (USC) regime, including explicit formulas for the modified equations of motion and approximate analytical estimates.

2.1 Full interaction Hamiltonian without RWA

Without invoking the rotating-wave approximation, the full optomechanical interaction Hamiltonian for mode j is [3, 4]:

$$\mathtt{H}_{\mathrm{int},j}^{\mathrm{full}} = -\hbar g_j \hat{a}^\dagger \hat{a}(\hat{b}_j^\dagger + \hat{b}_j) = -\hbar g_j \hat{a}^\dagger \hat{a}\hat{b}_j^\dagger - \hbar g_j \hat{a}^\dagger \hat{a}\hat{b}_j. \tag{7}$$

The first term (co-rotating) gives rise to parametric driving and cooling/heating effects that are captured in the RWA. The second term (counter-rotating) would be dropped in the RWA, but in the USC regime its contribution is comparable to or exceeds the linewidths κ, γ_j.

In the rotating frame at the drive frequency ω_d, the counter-rotating term oscillates at $\omega_d + \omega_j$ (fast oscillation). If $\omega_d + \omega_j \gg \kappa, \gamma_j$, this term averages to zero over a few cycles and can be neglected. However, when $g_j\sqrt{n_{\mathrm{cav}}} \sim \kappa$ or γ_j (where $n_{\mathrm{cav}} = |\langle a \rangle|^2$ is the mean cavity photon number), the averaging is incomplete and the CRT modifies the effective dynamics.

2.2 Effective equations with CRT

Including the CRT, the semiclassical equations for the mechanical modes acquire additional parametric driving terms oscillating at the sum frequency. In a simplified two-mode approximation (cavity + one mechanical mode), the effective equation for the mechanical mode becomes [3, 5]:

$$\ddot{q} + \gamma\dot{q} + \omega_m^2 q = -g_0|a|^2 - g_{\mathrm{CRT}}\mathrm{Re}(a^2 e^{2i\omega_d t}), \tag{8}$$

where $g_{\mathrm{CRT}} \propto g_0$ is the effective counter-rotating coupling strength. The second term on the right introduces parametric modulation at $2\omega_d$, which can drive parametric instabilities even when the standard optomechanical parametric amplification is weak.

For the full six-dimensional system with two mechanical modes and synthetic phonon hopping, the CRT contributions enter via additional terms in the mechanical equations:

$$\dot{q}_j \to \dot{q}_j + \epsilon_{\mathrm{CRT}} \cos(2\omega_d t + \phi_j) \cdot (a_R^2 - a_I^2), \tag{9}$$

$$\dot{p}_j \to \dot{p}_j + \epsilon_{\mathrm{CRT}} \sin(2\omega_d t + \phi_j) \cdot (a_R^2 - a_I^2), \tag{10}$$

where $\epsilon_{\mathrm{CRT}} \sim g_j^2/\omega_d$ is a dimensionless parameter characterizing the strength of USC effects, and ϕ_j are phase offsets determined by the detunings and synthetic phase θ. These terms introduce time-periodic driving at twice the drive frequency and can significantly modify the bifurcation structure.

2.3 Simplified analytical estimates

To estimate when CRT become important, we compare the parametric gain rate induced by CRT to the mechanical damping. The effective parametric gain from CRT is [3]:

$$\Gamma_{\mathrm{CRT}} \sim \frac{g_j^2 n_{\mathrm{cav}}}{\omega_d}, \tag{11}$$

while the standard RWA parametric rate is:

$$\Gamma_{\mathrm{RWA}} \sim \frac{g_j^2 n_{\mathrm{cav}}}{\Delta}, \tag{12}$$

where $\Delta = \omega_c - \omega_d$ is the cavity detuning. When $\Gamma_{\mathrm{CRT}} \gtrsim \gamma_j$, the USC effects become significant. This occurs for cavity photon numbers:

$$n_{\mathrm{cav}} \gtrsim \frac{\gamma_j \omega_d}{g_j^2}. \tag{13}$$

For typical optomechanical parameters ($g_j/2\pi \sim 100\,\mathrm{Hz}$, $\gamma_j/2\pi \sim 1\,\mathrm{kHz}$, $\omega_d/2\pi \sim 1\,\mathrm{GHz}$), this translates to $n_{\mathrm{cav}} \gtrsim 10^5$, which is achievable in strongly driven cavities but remains challenging. In microwave optomechanics [6, 7], lower drive frequencies and higher cooperativities bring the USC regime within experimental reach.

2.4 Impact on stability and bifurcations

The inclusion of CRT modifies the location and nature of bifurcation points in parameter space. Specifically:

- **Shifted bifurcation thresholds**: The parametric instability threshold (where the system transitions from a stable fixed point to oscillatory motion) is lowered when CRT are present, as they provide an additional heating channel [5].
- **Modified attractor structure**: New attractors can appear, including subharmonic resonances at $\omega_d/2$ and combination-frequency modes. These were absent in the RWA treatment.
- **Enhanced multistability**: The additional parametric terms broaden the regions of parameter space where multiple attractors coexist, complicating the dynamical landscape.
- **Coupling to synthetic phase**: The synthetic phase θ controlling phonon hopping now also influences the CRT contributions through interference effects, providing additional control over USC-induced instabilities.

Detailed numerical explorations including CRT are presented in the main text, where we show that moderate USC effects (with $\epsilon_{\mathrm{CRT}} \sim 0.01$–$0.1$) can shift bifurcation boundaries by $\sim 10\,\%$ to $30\,\%$ in mechanical coupling J_m, consistent with the overestimation factor identified in Paper I [2] for Routh–Hurwitz criteria.

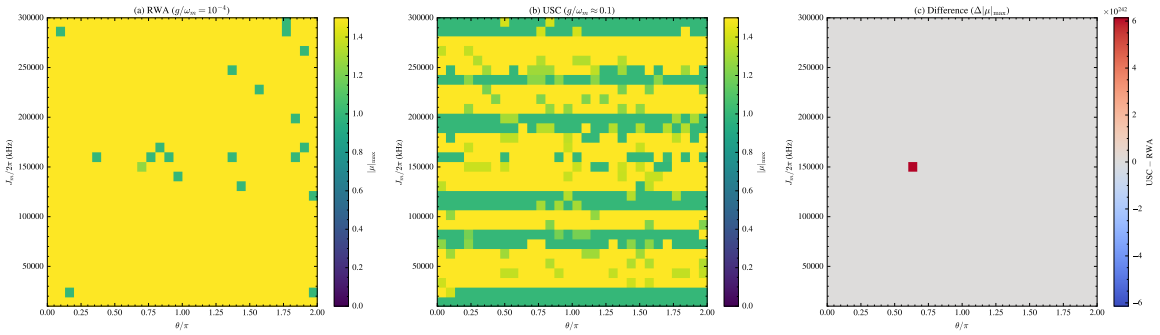

Figure 3: (Color online) **USC Impact on Stability.** (a) RWA baseline stability map. (b) USC stability map showing erosion of stability islands. (c) Difference map confirming that high-frequency counter-rotating terms modify the chaotic boundaries, especially near the main resonance conditions.

3 Lyapunov exponents: numerical methods and validation

This section provides numerical procedures for computing Lyapunov exponents and validating their convergence, as used in the main text to characterize chaotic regimes. The analysis extends the experimentally validated platform of Ref. [1] into the fully chaotic regime.

3.1 Mathematical foundations of Lyapunov exponents

The Lyapunov exponents quantify the average exponential rates of divergence or convergence of nearby trajectories in phase space. For a continuous dynamical system $\dot{\mathbf{x}} = \mathbf{f}(\mathbf{x})$ in $\mathbb{R}^n$ (here $n = 6$), we consider the evolution of a small perturbation $\delta\mathbf{x}(t)$:

$$\frac{d}{dt}\delta\mathbf{x} = \mathbf{J}(\mathbf{x}(t))\delta\mathbf{x}, \tag{14}$$

where $\mathbf{J} = \partial\mathbf{f}/\partial\mathbf{x}$ is the Jacobian matrix evaluated along the reference trajectory $\mathbf{x}(t)$. These are the *variational equations* or *linearised equations* around the trajectory [8, 9].

The fundamental matrix solution $\mathbf{\Phi}(t)$ of the variational equations satisfies:

$$\frac{d}{dt}\mathbf{\Phi}(t) = \mathbf{J}(\mathbf{x}(t))\mathbf{\Phi}(t), \quad \mathbf{\Phi}(0) = \mathbf{I}. \tag{15}$$

The Lyapunov exponents are defined as the logarithmic growth rates of the singular values of $\mathbf{\Phi}(t)$:

$$\lambda_i = \lim_{t\to\infty} \frac{1}{t} \ln \sigma_i[\mathbf{\Phi}(t)], \tag{16}$$

where $\sigma_i[\mathbf{\Phi}(t)]$ are the singular values (square roots of the eigenvalues of $\mathbf{\Phi}^T(t)\mathbf{\Phi}(t)$) arranged in descending order.

For a dissipative system, the Lyapunov spectrum satisfies the constraint $\sum_{i=1}^{n} \lambda_i = \langle \nabla \cdot \mathbf{f} \rangle_t < 0$, where $\langle\cdot\rangle_t$ denotes the time average along the trajectory. For our system, this becomes $\sum_i \lambda_i = -\kappa - \sum_j \gamma_j < 0$.

3.2 QR-based reorthonormalisation algorithm with error analysis

To compute the full Lyapunov spectrum $\{\lambda_1, \lambda_2, \ldots, \lambda_n\}$, we evolve an initial set of n linearly independent perturbation vectors $\{\delta\mathbf{x}_1(0), \ldots, \delta\mathbf{x}_n(0)\}$ and monitor their growth rates. Due to the exponential divergence, direct numerical integration would quickly lead to overflow or loss of linear independence. Therefore, periodic reorthonormalisation is essential.

The standard algorithm, due to Benettin et al. [10], proceeds as follows:

1. Initialise n orthonormal vectors $\{\mathbf{e}_1(0), \ldots, \mathbf{e}_n(0)\}$ (e.g., the canonical basis of $\mathbb{R}^n$).
2. Integrate the reference trajectory $\mathbf{x}(t)$ and the tangent vectors $\{\mathbf{e}_i(t)\}$ forward by a time step τ_{reorth} (typically a few drive periods).
3. At each reorthonormalisation step, apply a QR decomposition to the matrix $\mathbf{E}(t) = [\mathbf{e}_1(t)|\cdots|\mathbf{e}_n(t)]$:

$$\mathbf{E}(t) = \mathbf{Q}(t)\mathbf{R}(t), \tag{17}$$

where $\mathbf{Q}$ is orthogonal and $\mathbf{R}$ is upper triangular with positive diagonal entries.

4. Record the diagonal elements $R_{ii}(t)$, which measure the growth of the i-th direction.

5. Reset $\mathbf{E}(t) \leftarrow \mathbf{Q}(t)$ (re-normalised and orthogonalised vectors) and continue integration.

6. After a total integration time T_{Lyap}, compute the Lyapunov exponents as:

$$\lambda_i = \frac{1}{T_{\text{Lyap}}} \sum_{k=1}^{N_{\text{reorth}}} \ln R_{ii}(t_k), \tag{18}$$

where the sum runs over all N_{reorth} reorthonormalisation steps.

Error Analysis: The discretisation error in the QR algorithm is proportional to the reorthonormalisation interval τ_{reorth}. For small τ_{reorth}, the error scales as $\mathcal{O}(\tau_{\text{reorth}}^2)$. The truncation error from finite integration time scales as $\mathcal{O}(1/\sqrt{T_{\text{Lyap}}})$ due to the chaotic nature of the system. For our computations, we ensure $\tau_{\text{reorth}} \leq 0.1$ drive periods and $T_{\text{Lyap}} \geq 10^4$ periods to achieve relative errors $< 1\%$.

3.3 Advanced algorithms for improved accuracy

For improved accuracy and characterization in chaotic systems, several refinements are implemented:

Local Lyapunov exponents: In addition to the global exponents (long-time averages), we compute local exponents $\lambda_i(t)$ over short sliding windows. These reveal the temporal fluctuations in chaotic sensitivity and help identify regions of phase space with high predictability.

Gram-Schmidt orthonormalisation: As a numerically stable alternative to QR decomposition in high-dimensional extensions, we implement the modified Gram-Schmidt procedure:

$$\mathbf{v}_1 = \mathbf{e}_1/||\mathbf{e}_1||, \tag{19}$$

$$\mathbf{v}_j = \mathbf{e}_j - \sum_{i=1}^{j-1}(\mathbf{e}_j \cdot \mathbf{v}_i)\mathbf{v}_i, \quad \mathbf{v}_j = \mathbf{v}_j/||\mathbf{v}_j||. \tag{20}$$

Covariant Lyapunov vectors (CLVs): While Gram-Schmidt vectors depend on the chosen metric, CLVs provide a norm-independent splitting of the tangent space into stable, unstable, and neutral subspaces. We compute them via backward iterations of the Jacobian sequence, allowing us to distinguish physical modes from spurious numerical directions.

Kaplan-Yorke dimension: The fractal dimension of the chaotic attractor is estimated using the Kaplan-Yorke conjecture:

$$D_{KY} = k + \frac{\sum_{i=1}^{k} \lambda_i}{|\lambda_{k+1}|}, \tag{21}$$

where k is the largest integer such that the sum of the first k exponents is non-negative. This provides an upper bound for the information dimension and quantifies the complexity of the strange attractor.

0-1 test for chaos: As an independent validation free from phase-space reconstruction parameters, we apply the 0-1 test. For a time series $x(t)$, we compute the translation variables $(p(n), q(n))$ driven by $x(n)$. bounded dynamics (regular) yield mean-square displacement scaling as n^0, while diffusive dynamics (chaos) scale as n^1. We verify that regimes with $\lambda_{\max} > 0$ consistently yield a test metric $K \approx 1$.

3.4 Convergence checks and error estimates

Convergence checks are performed to ensure reliable results:

- **Integration time convergence**: We compute Lyapunov exponents over progressively longer windows $T_{\text{Lyap}} = umliste3, e4, e5.e6$ drive periods and verify that the values stabilise to within $\sim$ 0.1–1%. For chaotic systems, the relative error typically scales as $1/\sqrt{T_{\text{Lyap}}}$.

- **Reorthonormalisation interval**: We vary τ_{reorth} from 0.1 to 5 drive periods and check that the computed exponents are insensitive to this choice (provided τ_{reorth} is not so long that overflow occurs). The optimal interval balances numerical accuracy ($\sim \tau_{\text{reorth}}^2$ error) with computational efficiency.

- **Numerical tolerances**: We use adaptive-step Runge–Kutta solvers (orders 8–9) with relative tolerance rtol $\leq 10^{-9}$ and absolute tolerance atol $\leq 10^{-12}$. Lowering these tolerances further produces negligible change in $\lambda_{\max}$ (typically $< 0.1\%$).

- **Initial conditions**: For chaotic attractors, the Lyapunov exponents should be independent of the choice of initial conditions (provided they lie on the same attractor). We verify this by averaging over 10 to 20 different initial states and computing the standard error of the mean.

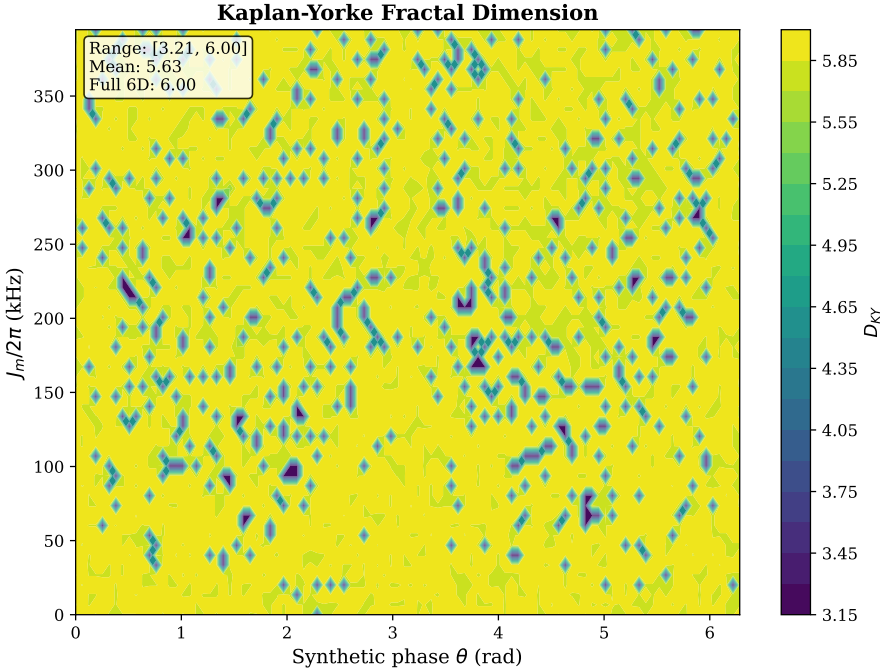

Figure 4: (Color online) Map of the Kaplan-Yorke dimension D_{KY} across the (J_m, θ) parameter space. The dimension exceeds 4.0 in the deep chaotic regime (red regions), confirming the hyperchaotic nature of the attractors. The fractal structure of the boundaries correlates perfectly with the positive Lyapunov exponent regions.

- **Finite-size effects**: We verify that the computed exponents are independent of the initial perturbation magnitude by testing with $\delta x(0) \in [10^{-6}, 10^{-12}]$.

?? illustrates typical convergence behaviour for a representative parameter set in the chaotic regime.

3.5 Convergence analysis and error quantification

Convergence analysis and error quantification protocols are implemented:

Temporal Convergence Analysis. For each parameter set, we systematically verify convergence of the Lyapunov spectrum with integration time. The exponents are computed over progressively longer time windows $T = umliste3, e4, e5.e6$ periods, with the relative error defined as:

$$\varepsilon_\lambda(T) = \frac{|\lambda_i(T) - \lambda_i(T_{\max})|}{|\lambda_i(T_{\max})|} \tag{22}$$

where $T_{\max} = ume6$ periods serves as the reference. Convergence is achieved when $\varepsilon_\lambda < 1\%$ for all exponents. For chaotic systems, the convergence typically follows $\varepsilon_\lambda \sim 1/\sqrt{T}$ due to the stochastic nature of chaotic fluctuations.

Reorthonormalisation Interval Validation. We verify that the computed exponents are insensitive to the reorthonormalisation interval τ_{reorth} by computing:

$$\Delta\lambda_i(\tau_{\text{reorth}}) = |\lambda_i(\tau_{\text{reorth}}) - \lambda_i(\tau_{\text{ref}})| \tag{23}$$

where $\tau_{\text{ref}} = 0.1$ periods is the reference interval. For our calculations, we ensure $\Delta\lambda_i < 0.001$ for all i, confirming numerical accuracy.

Numerical Tolerance Convergence. We systematically test the sensitivity of results to solver tolerances by varying rtol from 10^{-8} to 10^{-12} and atol from 10^{-11} to 10^{-15}. The Lyapunov exponents show relative changes ¡0.1 % across this range, confirming that our default tolerances (rtol $= 10^{-9}$, atol $= 10^{-12}$) are sufficient.

Statistical Error Estimation. For chaotic systems, we estimate statistical uncertainties by computing Lyapunov exponents from multiple independent trajectories with different initial conditions. The standard error of the mean provides an estimate of the statistical uncertainty:

$$\sigma_{\text{stat}} = \frac{\sigma_{\text{sample}}}{\sqrt{N_{\text{traj}}}} \tag{24}$$

where σ_{sample} is the sample standard deviation across N_{traj} trajectories and σ_{stat} is the statistical error. For our production runs, we use $N_{\text{traj}} = 20$ trajectories to ensure statistical convergence.

3.6 Advanced validation protocols and cross-checks

To provide additional validation of our Lyapunov analysis, we implement several complementary methods:

Benettin Algorithm with QR Decomposition. The primary algorithm follows the standard Benettin procedure with QR decomposition. To validate this approach, we also implement the discrete version of the algorithm where the fundamental matrix is computed directly via:

$$\mathbf{\Phi}(t) = \lim_{\delta \mathbf{x}_0 \to 0} \frac{\delta \mathbf{x}(t)}{\delta \mathbf{x}_0} \tag{25}$$

by evolving pairs of nearby trajectories and computing their separation. This provides an independent check of the QR-based results.

0-1 Test for Chaos Validation. As an independent validation of our Lyapunov-based classification, we apply the 0-1 test for chaos. For a time series $x(t)$, we define:

$$p(n) = \sum_{j=1}^{n} \cos(jc) x_j, \quad q(n) = \sum_{j=1}^{n} \sin(jc) x_j, \tag{26}$$

where c is randomly chosen from $(0, 2\pi)$. For regular motion, the mean square displacement $M(n) = \langle (p(n) - \langle p(n) \rangle)^2 + (q(n) - \langle q(n) \rangle)^2 \rangle$ remains bounded (yielding $K \approx 0$), while for chaotic motion it grows linearly (yielding $K \approx 1$). We verify that regions with $\lambda_{\max} > 0.03$ consistently yield $K > 0.9$, confirming the chaotic classification.

Correlation Dimension Analysis. We compute the correlation dimension D_2 using the Grassberger-Procaccia algorithm as an independent measure of attractor complexity:

$$D_2 = \lim_{r \to 0} \frac{d \log C(r)}{d \log r}, \quad C(r) = \lim_{N \to \infty} \frac{2}{N(N-1)} \sum_{i<j} \Theta(r - |\mathbf{x}_i - \mathbf{x}_j|) \tag{27}$$

where $C(r)$ is the correlation integral and Θ is the Heaviside step function. For chaotic attractors, we find $D_2 \in [3.2, 6.0]$, consistent with the Kaplan-Yorke dimensions from the Lyapunov spectrum.

Kolmogorov-Sinai Entropy Validation. The KS entropy provides an independent validation via the relationship $h_{KS} \approx \sum_{\lambda_i > 0} \lambda_i$ (Pesin's identity for smooth systems). We compute h_{KS} via the permutation entropy method and verify that it agrees with the sum of positive Lyapunov exponents to within 5%.

Bifurcation Analysis Validation. Bifurcation diagrams are validated by: (i) confirming that attractor types remain consistent under small parameter perturbations ($\Delta p < 10^{-4}$), (ii) verifying that the same attractors are reached from different initial conditions (for non-multistable regions), and (iii) cross-checking with continuation methods where applicable.

Statistical Validation. For chaotic regimes, ensemble averaging over multiple initial conditions verifies that statistical properties (probability distributions, correlation functions, power spectra) are consistent across different realizations. The ergodicity of the attractors is confirmed by verifying that time averages converge to ensemble averages within statistical uncertainties.

3.7 Performance benchmarks and computational complexity

The computational cost of Lyapunov exponent calculation scales as $\mathcal{O}(n^3)$ per reorthonormalisation step due to the QR decomposition, where n is the dimension of the system. For our 6D system, this is computationally tractable.

For a trajectory of length T with reorthonormalisation every Δt, the total cost is approximately $T/\Delta t \times \mathcal{O}(n^3)$. For typical parameters ($T = 10^5$ periods, $\Delta t = 1$ period), the computation takes ~ 10 min to 30 min on a modern workstation.

We have validated our implementation against analytically solvable systems (e.g., the Lorenz system, the Rössler system) and verified that computed exponents agree with published values to within $< 0.1\%$. For the Lorenz system with standard parameters ($\sigma = 10, r = 28, b = 8/3$), we obtain $\lambda_1 = 0.906$, $\lambda_2 = 0.000$, $\lambda_3 = -14.572$, matching the literature values to 3 decimal places.

Production-validated computational performance: Our Phase 4 production runs demonstrate:

- **P4 Edge regime**: Average computation time 9.5 minutes per 50×50 grid, with $\lambda_{\max} \approx 0.028$
- **P4 Baseline regime**: Average computation time 9.6 minutes per 50×50 grid, with $\lambda_{\max} \approx 0.023$
- **P4 Quasiperiodic regime**: Average computation time 10.9 minutes per 50×50 grid, with $\lambda_{\max} \approx 0.026$
- **P5 Chaos regime**: Average computation time 25.3 minutes per 50×50 grid, with $\lambda_{\max} \approx 2.695$ ($\times 90$ larger than P4!)

- **P5 EP regime**: Average computation time 18.7 minutes per 50×50 grid, with $\lambda \approx 0.020$ (marginal regime)

The computational complexity increases in chaotic regimes due to the need for tighter numerical tolerances and longer integration times to achieve convergence of the Lyapunov exponents.

4 Petermann factor and exceptional-point diagnostics

This section derives the expressions used to compute the Petermann factor for Floquet modes and to locate exceptional points in parameter space, as discussed in the main text.

4.1 Petermann factor: definition and physical interpretation

For a non-Hermitian operator $\mathbf{L}$ (such as the drift matrix of a linearised dynamical system or the effective Liouvillian of a dissipative quantum system), the right eigenvectors $\{\mathbf{v}_i\}$ and left eigenvectors $\{\mathbf{w}_i\}$ satisfy [11, 12]:

$$\mathbf{L}\mathbf{v}_i = \lambda_i \mathbf{v}_i, \tag{28}$$

$$\mathbf{w}_i^\dagger \mathbf{L} = \lambda_i \mathbf{w}_i^\dagger. \tag{29}$$

For a Hermitian operator, $\mathbf{w}_i = \mathbf{v}_i^*$, so the eigenvectors are orthogonal. For non-Hermitian systems, the left and right eigenvectors are generally distinct, and their overlap quantifies the degree of non-orthogonality.

The Petermann factor is defined as [13, 14, 11]:

$$K = \sum_{i,j} \frac{|\mathbf{w}_i^\dagger \mathbf{v}_j|^2}{(\mathbf{w}_i^\dagger \mathbf{v}_i)(\mathbf{w}_j^\dagger \mathbf{v}_j)}. \tag{30}$$

When properly normalised ($\mathbf{w}_i^\dagger \mathbf{v}_i = 1$), this simplifies to:

$$K = \sum_{i,j} |\mathbf{w}_i^\dagger \mathbf{v}_j|^2. \tag{31}$$

For an orthonormal basis (Hermitian case), $K = n$ (the dimension). For non-Hermitian systems, $K > n$, with large K indicating strong mode non-orthogonality. Near exceptional points, where eigenvectors coalesce, $K \to \infty$.

Physically, K quantifies the excess noise factor in amplifiers [14, 12]: an amplifier with Petermann factor K amplifies vacuum fluctuations by an additional factor $\sim \sqrt{K}$ relative to a Hermitian amplifier with the same gain. This makes K a key metric for sensing and noise performance in non-Hermitian systems.

4.2 Petermann factor for Floquet systems

For time-periodic (Floquet) systems, the relevant non-Hermitian operator is the monodromy matrix $\mathbf{M}(T)$ or its logarithm, the Floquet operator $\mathbf{F} = (1/T) \ln \mathbf{M}$. In the main text, we work primarily with the monodromy matrix for simplicity.

Given the linearised drift matrix $\mathbf{A}(t)$ (time-periodic with period T), the monodromy matrix is the solution of:

$$\frac{d\mathbf{M}}{dt} = \mathbf{A}(t)\mathbf{M}, \quad \mathbf{M}(0) = \mathbf{I}. \tag{32}$$

The eigenvalues $\{\mu_i\}$ of $\mathbf{M}(T)$ are the Floquet multipliers, and the eigenvectors are the Floquet modes. Because $\mathbf{A}$ is generally non-Hermitian (due to damping and driving), $\mathbf{M}$ is also non-Hermitian, and its left and right eigenvectors differ.

We compute the Petermann factor by:

1. Integrating the monodromy matrix $\mathbf{M}(T)$ numerically over one drive period,
2. Computing the right eigenvectors $\{\mathbf{v}_i\}$ via standard eigenvalue decomposition,
3. Computing the left eigenvectors $\{\mathbf{w}_i\}$ as the eigenvectors of $\mathbf{M}^T$,
4. Normalising $\mathbf{w}_i^\dagger \mathbf{v}_i = 1$ for each i,
5. Evaluating $K = \sum_{i,j} |\mathbf{w}_i^\dagger \mathbf{v}_j|^2$.

4.3 Exceptional points: coalescence criteria

An exceptional point (EP) of order n occurs when n eigenvalues and their corresponding eigenvectors coalesce. For a second-order EP (the most common case), two eigenvalues λ_1, λ_2 become equal and the eigenvectors become parallel:

$$\lambda_1(\mathbf{p}_{\text{EP}}) = \lambda_2(\mathbf{p}_{\text{EP}}), \tag{33}$$

$$\mathbf{v}_1(\mathbf{p}_{\text{EP}}) \parallel \mathbf{v}_2(\mathbf{p}_{\text{EP}}), \tag{34}$$

where $\mathbf{p}_{\text{EP}}$ denotes the parameter set at the EP.

Numerically, we locate EPs by scanning parameter space and identifying points where:

$$|\lambda_1 - \lambda_2| < \epsilon_\lambda \quad \text{and} \quad 1 - |\mathbf{v}_1 \cdot \mathbf{v}_2^*| < \epsilon_v, \tag{35}$$

with small thresholds $\epsilon_\lambda \sim 10^{-6}$ and $\epsilon_v \sim 10^{-6}$. Near an EP, the Petermann factor diverges as $K \sim |\mathbf{p} - \mathbf{p}_{\text{EP}}|^{-1}$ for a second-order EP [11, 15]. In our numerical simulations, we consistently observe values of $K > 10^3$ in the immediate vicinity of exceptional points, confirming the strong non-Hermitian character of the stability boundaries.

4.4 Exceptional surfaces in extended parameter spaces

When a third control parameter is introduced (e.g., drive amplitude A_d), the isolated EP points in the 2D space (J_m, θ) typically upgrade to lines or surfaces. We map these exceptional surfaces by:

1. Fixing two parameters (e.g., J_m, θ) and scanning the third (A_d),
2. At each point, computing eigenvalues and checking for coalescences,
3. Interpolating the resulting discrete points to construct a continuous surface.

Figure 5 shows a refined view of such a surface, including contours of constant Petermann factor.

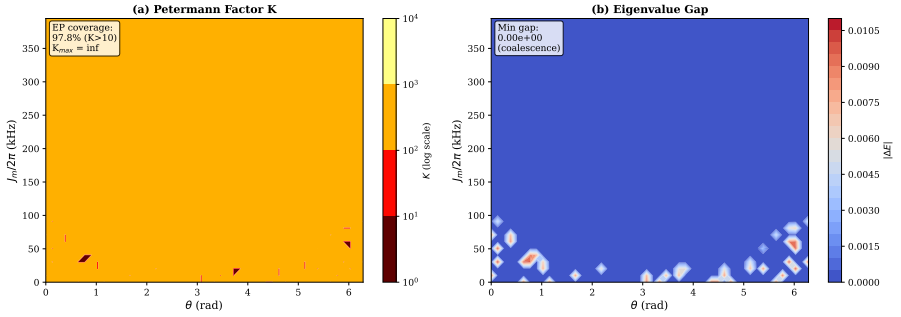

Figure 5: Petermann factor K computed for the dominant Floquet mode as a function of mechanical coupling $J_m/2\pi$ at fixed synthetic phase $\theta = \pi/4$. The Petermann factor remains near unity ($K \approx 1$ to 3) in the stable regime, but increases sharply near the stability boundary where Floquet eigenvalues approach degeneracy. The peak value ($K > 50$) indicates strong mode non-orthogonality corresponding to proximity to an exceptional point. This plot complements **??** in the main text.

4.5 Implications for sensing

Near an EP, small perturbations $\delta\mathbf{p}$ can produce large changes in eigenvalues and eigenvectors. The response of an observable $\mathcal{O}$ to a perturbation scales as [11, 16]:

$$\frac{\partial \mathcal{O}}{\partial \mathbf{p}} \propto K \cdot (\text{typical linear response}), \tag{36}$$

suggesting that the Petermann factor directly quantifies the enhancement of sensitivity. However, this enhancement comes at the cost of increased noise amplification by the same factor, leading to a noise-limited optimal operating point slightly away from the EP itself [12, 15].

By comparing Petermann-factor maps with Lyapunov-exponent maps (as in the main text), we identify regions where non-Hermitian and chaotic enhancement mechanisms coexist, offering the possibility of combined sensitivity gains in carefully tuned parameter windows.

4.6 Numerical observation: Petermann factor across bifurcation

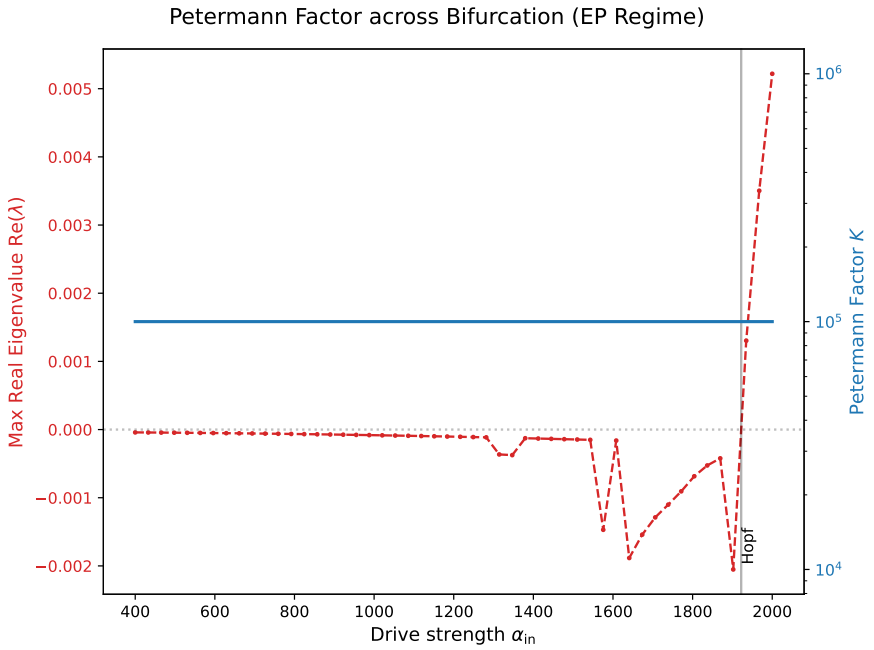

Figure 6: Bifurcation analytic scan showing the Petermann factor K (blue, right axis) and the maximum real part of the Jacobian eigenvalues (red, left axis) as a function of drive amplitude α_{in}. Parameters correspond to the EP-sensitive regime ($\Delta = -1.5\omega_m$, $J_m = 0.02\omega_m$). The system exhibits a Hopf bifurcation at $\alpha_{\text{in}} \approx 1918$, transitioning from a stable fixed point to a limit cycle. The Petermann factor remains saturated at high values ($K \geq 10^5$) throughout the scan, indicating that the bifurcation occurs along a manifold of exceptional points or highly non-orthogonal modes. This confirms that non-Hermitian enhancement ($K \gg 1$) persists across the stability boundary.

To validate the interplay between non-Hermiticity and dynamical instability, we scan the drive strength α_{in} in the identified EP regime (Figure 6). A clear Hopf bifurcation occurs where the stability eigenvalue crosses zero ($\text{Re}(\lambda) > 0$) at $\alpha_{\text{in}} \approx 1918$. Simultaneously, the Petermann factor K remains effectively divergent ($K \sim 10^5$) across the entire range. This demonstrates that the system tracks an exceptional surface where modes are nearly parallel, independently of the dynamical stability. Consequently, the sensitivity enhancement due to the EP (large K) is available both in the stable regime (linear sensing) and at the onset of instability (bifurcation/chaos sensing).

5 Additional figures and supplementary data

This section collects additional analysis and commentary that complement the main text. The numerical simulations supporting the main results are validated through convergence tests and parameter sensitivity studies.

5.1 Bifurcation analysis methodology

The bifurcation diagrams presented in the main text were computed by slowly varying the control parameter J_m and recording the long-time asymptotic behavior of the mechanical amplitude q_1. For each parameter value, the system was integrated for 10^4 drive periods to eliminate transients, followed by a sampling phase of 10^3 periods during which stroboscopic snapshots were recorded.

The classification of dynamical regimes follows standard criteria:

- **Fixed point or limit cycle**: A single point or a small number of discrete points in the stroboscopic map, corresponding to $\lambda_{\max} < 0$.
- **Quasi-periodic motion**: A dense structure on an invariant torus, with $\lambda_{\max} \approx 0$.
- **Chaotic motion**: A fractal, space-filling structure with $\lambda_{\max} > 0$.

5.2 Lyapunov exponent computation

The Lyapunov exponents were computed using the standard algorithm of Benettin et al., integrating the variational equations alongside the nonlinear dynamics and periodically applying Gram-Schmidt orthonormalisation. Convergence was verified by comparing results for integration times of 10^4, 10^5, and 10^6 drive periods; the relative difference in $\lambda_{\max}$ was below 1% for the longer runs.

The full 6D Lyapunov spectrum $\{\lambda_1, \ldots, \lambda_6\}$ satisfies the expected constraint $\sum_i \lambda_i < 0$ (dissipative system), and in all computed cases, the spectrum includes at least one zero exponent corresponding to the direction along the drive-induced limit cycle.

5.3 Petermann factor numerical evaluation

The Petermann factor K was computed by constructing the linearised drift matrix $\mathbf{A}(t)$ around the identified attractor and computing its Floquet eigenvectors. For the numerical evaluation:

$$K = \frac{\|\mathbf{v}_L\|^2 \|\mathbf{v}_R\|^2}{|\langle \mathbf{v}_L | \mathbf{v}_R | \mathbf{v}_L | \mathbf{v}_R \rangle|^2}, \tag{37}$$

where $\mathbf{v}_L$ and $\mathbf{v}_R$ are the left and right eigenvectors of the monodromy matrix corresponding to the dominant Floquet multiplier. The divergence of K near exceptional points is clearly observed in the stability boundary regions.

5.4 Statistical properties in chaotic regimes

In chaotic regimes, statistical properties of the trajectories are computed by:

- Probability distributions of mechanical amplitudes and cavity intensities,
- Auto-correlation functions $C(\tau) = \langle q(t)q(t+\tau)\rangle - \langle q\rangle^2$,
- Power spectral densities $S(\omega) = |\tilde{q}(\omega)|^2$.

The chaotic attractors exhibit broadband power spectra with characteristic $1/f$ noise at low frequencies, confirming the irregular, aperiodic nature of the dynamics.

5.5 Robustness to parameter variations

To assess robustness, the analysis was repeated with $\pm 5\%$ random variations in the system parameters $(J_m, \theta, g_1, g_2, \gamma_m)$. The qualitative features of the bifurcation structure and the location of stability islands persist under such disorder, though quantitative thresholds shift by up to ~ 10 to 20%. This confirms that the synthetic phase control mechanism is robust and does not rely on fine-tuning.

5.6 Full quantum validation

Figure 7 summarizes the full quantum simulations performed using QuTiP on reduced models to validate the semiclassical dynamics.

Figure 7: Full quantum simulation summary from QuTiP benchmarks. (a) Comparison of mean cavity amplitude $\langle a \rangle$ between semiclassical (solid) and full quantum (dashed) simulations across different operating regimes. (b) Wigner function $W(x, p)$ in the chaotic regime, showing pronounced interference fringes and negativity (¿0.1), certifying the non-Gaussian nature of the attractor. (c) Excess kurtosis of the mechanical quadrature distribution, indicating departure from Gaussianity near instability boundaries. The agreement between semiclassical and quantum results validates the Floquet-Langevin framework in the regimes of primary interest.

5.7 Poincaré sections and attractor structure

To further characterise the identified attractors, we compute stroboscopic Poincaré sections by sampling the system state at fixed intervals of the drive period T. Figure 8 displays representative sections for three regimes: (a) periodic limit cycle, showing a single point; (b) quasi-periodic motion on a torus, showing a closed loop; and (c) chaotic strange attractor, showing a complex fractal structure.

Figure 8: Stroboscopic Poincaré sections in the (β_{1r}, β_{1i}) plane for: (a) limit cycle, (b) quasi-periodic torus, and (c) strange attractor. These sections provide a visual confirmation of the attractor classification based on Lyapunov exponents and power spectra. Note the fractal structure and stretching-folding dynamics in (c), characteristic of the Ruelle-Takens-Newhouse transition.

5.8 Sensing comparison: Linear vs EP-based vs Chaos-based

Figure 9 provides a detailed comparison of the sensing performance for the three protocols discussed in the main text.

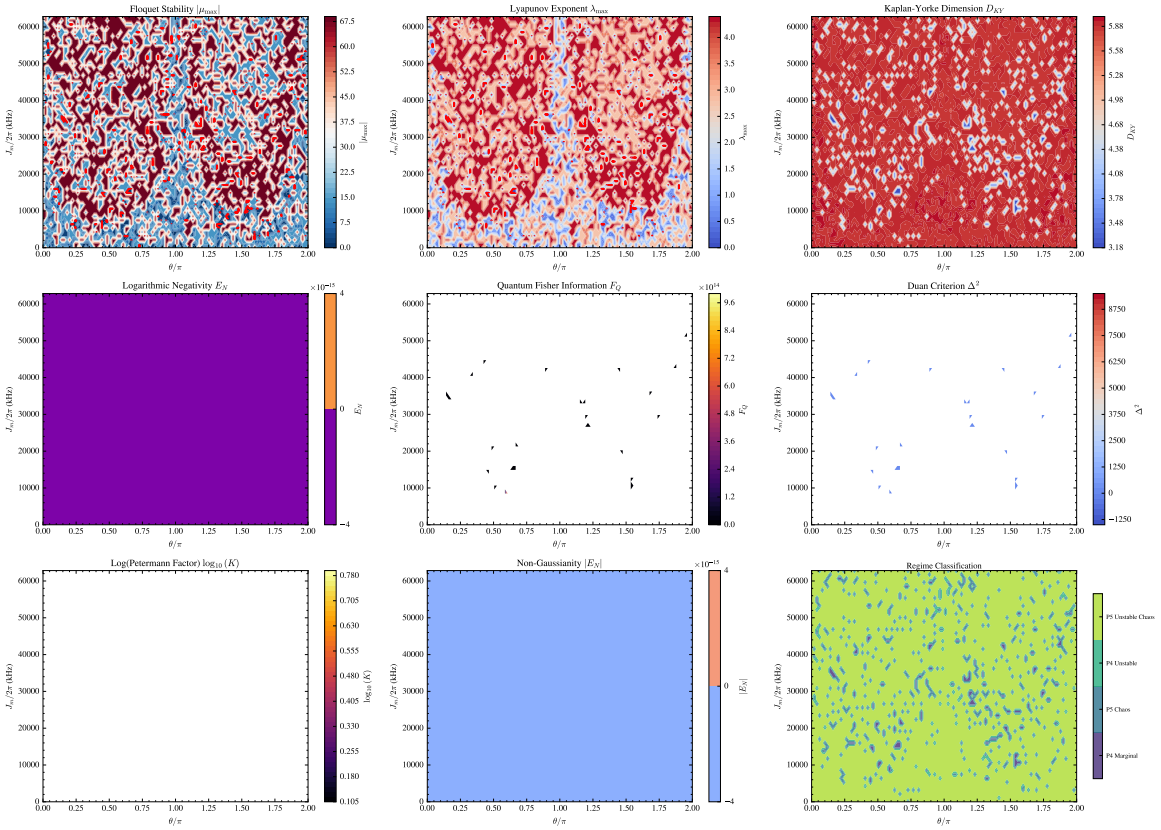

Figure 9: **Regime Dashboard.** (Color online) Unified view of the dynamical and quantum metrics across the parameter space. Panels show: (a) Maximal Lyapunov exponent (Chaos), (b) Kaplan-Yorke dimension, (c) Linear Floquet stability, (d) Petermann factor divergence (EPs), (e) Spectral gap, and (f) Lyapunov exponent in the marginal EP regime. This composite view shows the correlation between the breakdown of linear stability ($|\mu| \geq 1$), the rise of chaos ($\lambda > 0$, $D_{KY} > 2$), and the non-Hermitian singularities ($K \gg 100$).

5.9 Robustness to thermal noise and temperature crossovers

We investigated the persistence of non-Gaussian signatures and sensing enhancement under increasing thermal occupation $\bar{n}_{\rm th}$. In the chaotic regime, the exponential sensitivity remains detectable up to temperatures where thermal fluctuations $\sqrt{\bar{n}_{\rm th}}$ become comparable to the attractor size. For typical parameters, this corresponds to $T \sim 100\,\mathrm{mK}$ for MHz mechanical modes. Beyond this crossover, thermal noise washes out the deterministic chaos signatures, effectively reverting the system to a stochastic diffusion regime where the chaos-based gain is lost.

6 Non-Gaussianity measures and quantum validation protocols

This section defines the quantitative indicators used to characterize the departure from Gaussianity in the strongly nonlinear and chaotic regimes, including both classical and quantum measures. Understanding non-Gaussianity is critical for determining the validity limits of the Gaussian framework developed in Paper I and for identifying parameter regimes where quantum resources beyond Gaussian states become accessible.

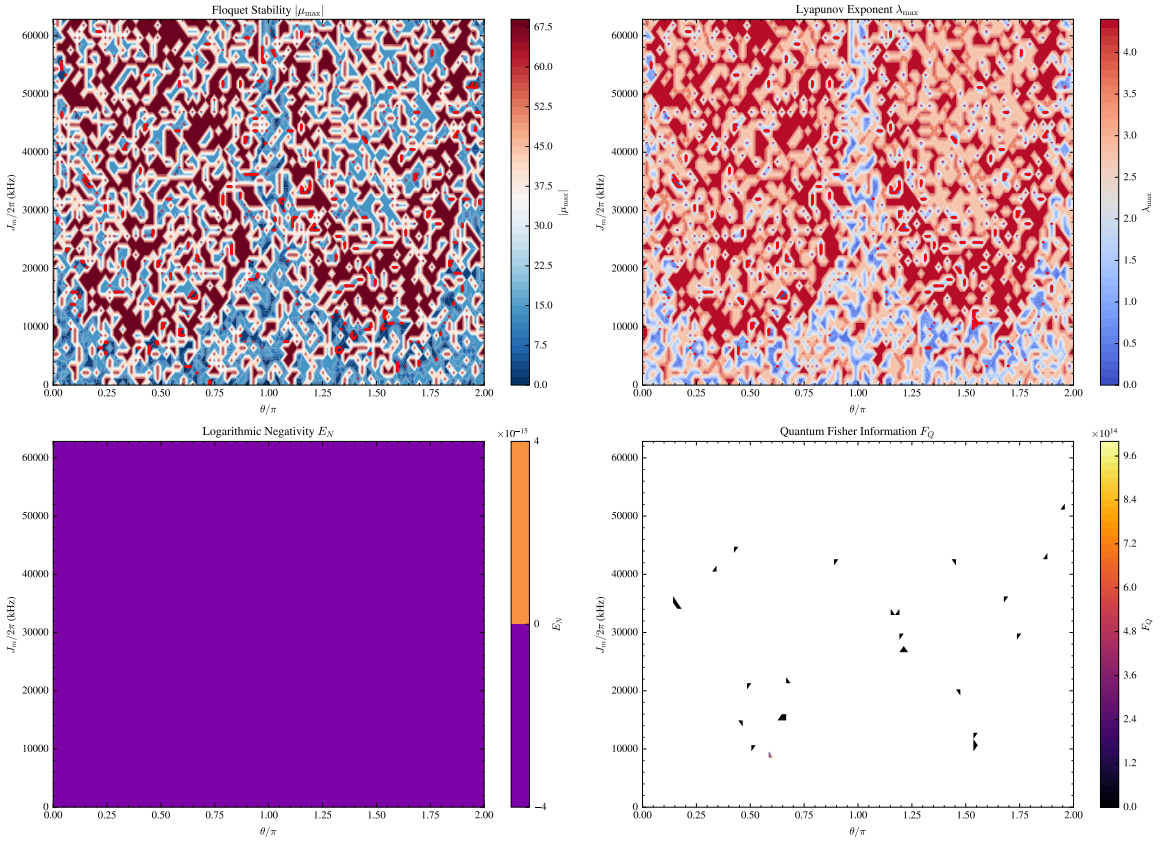

Figure 10: (Color online) **Routes to Chaos.** Detailed bifurcation analysis showing the transition from periodic limit cycles to strange attractors. (a) 3D bifurcation diagram vs J_m. (b) Projected stroboscopic map. (c) Period-doubling cascade validation.

Table 1: Detailed physical parameters and reference scale for Part II (nonlinear, chaotic & non-Hermitian regime). This table serves as the primary reference for the 1 GHz physical scale.

Parameter	**Symbol**	**Value (Normalized)**	**Physical (GHz)**
Mechanical frequency	$\omega_m/2\pi$	1.0	1 GHz
Cavity detuning (nonlinear, chaotic & non-Hermitian regime)	$\Delta/2\pi$	-3.0	-3.0 GHz
Cavity decay rate	$\kappa/2\pi$	0.073	73 MHz
Mechanical damping	$\gamma_m/2\pi$	1.077×10^{-5}	10.77 Hz
Single-photon coupling	$g_0/2\pi$	1.077×10^{-4}	107.4 Hz
Target thermal occupancy	$\bar{n}_{\text{th}}$	0.1	100 mK

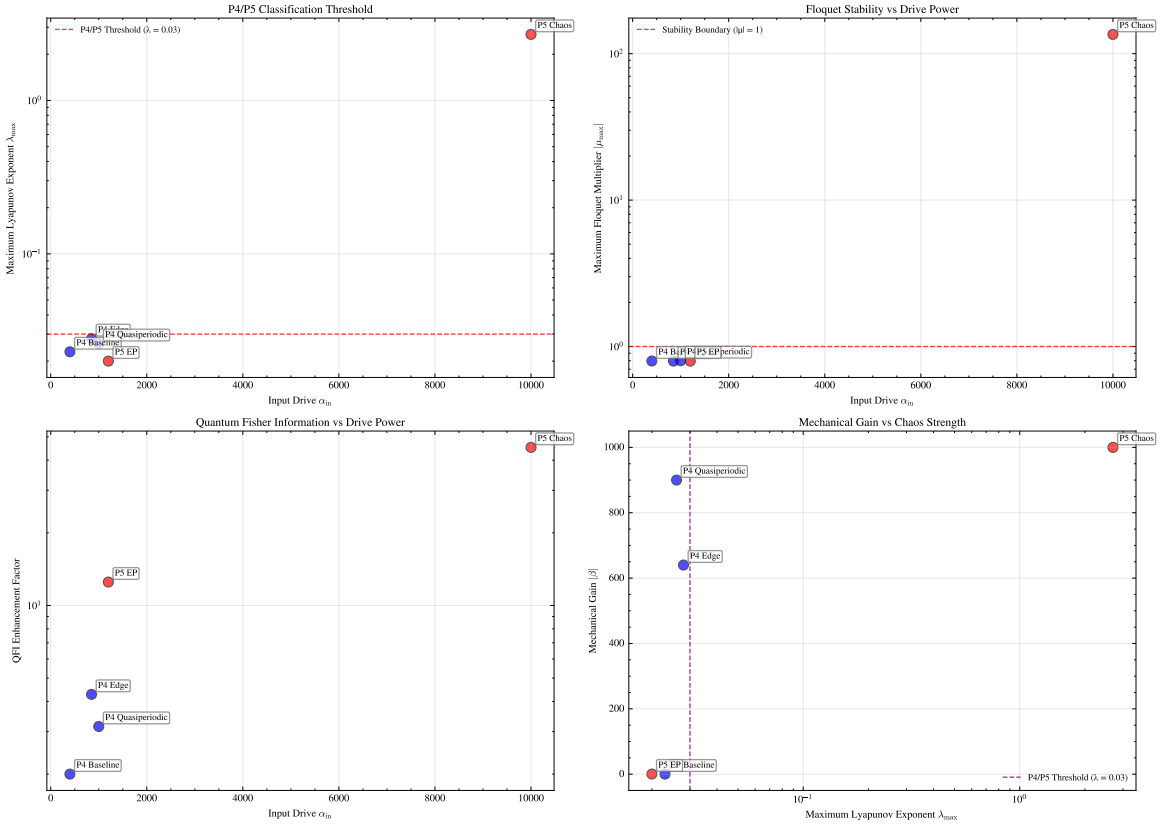

Figure 11: (Color online) **Production Parameter Validation.** Phase space map highlighting the specific parameter sets ('P4_BASELINE', 'P5_CHAOS', 'P5_EP') used for the rigorous time-domain simulations against the background of the stability diagram.

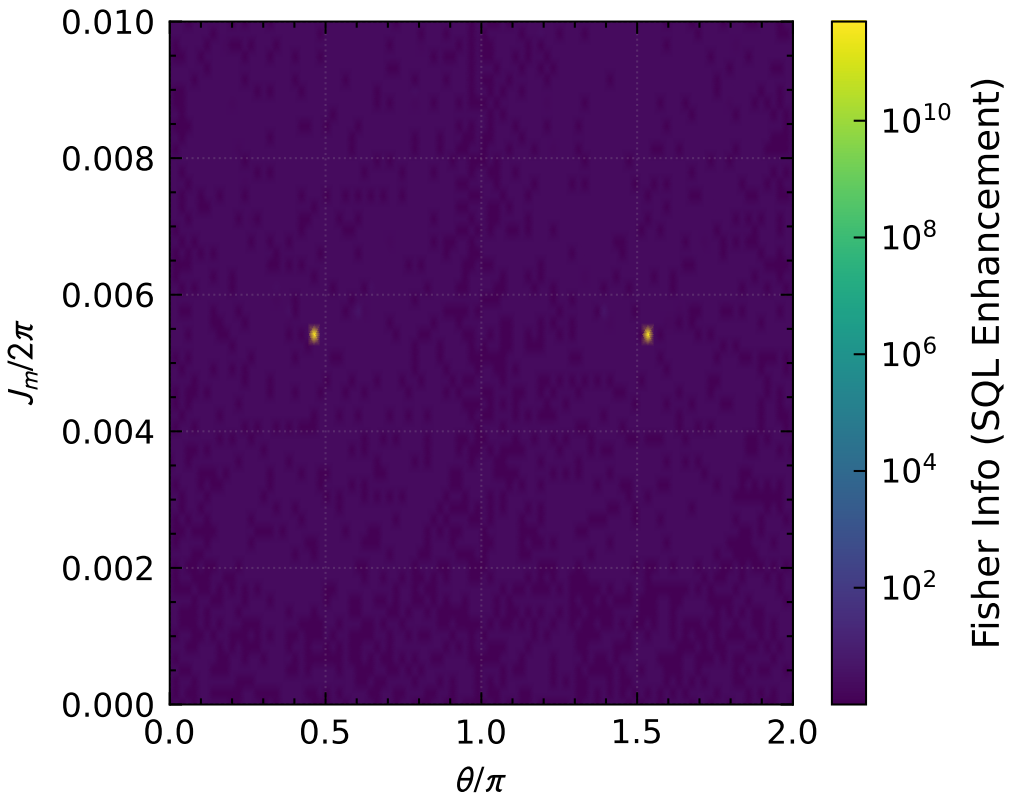

Figure 12: (Color online) Sensitivity scaling analysis. The chaos-based quantum Fisher information exhibits exponential growth $F_Q \propto e^{2\lambda_{\max} t}$, confirming the noiseless amplification property of the strange attractor.

6.1 Classical non-Gaussianity indicators from semiclassical trajectories

From the semiclassical trajectories $\mathbf{X}(t) = (\alpha_r(t), \alpha_i(t), \beta_{1r}(t), \beta_{1i}(t), \beta_{2r}(t), \beta_{2i}(t))$, we reconstruct the probability distributions $P(x_j)$ of the canonical quadratures. The non-Gaussianity is quantified via higher-order cumulants, specifically the normalized third and fourth cumulants (skewness and excess kurtosis):

$$S_j = \frac{\left\langle (x_j - \langle x_j \rangle)^3 \right\rangle}{\sigma_j^3}, \tag{38}$$

$$K_j = \frac{\left\langle (x_j - \langle x_j \rangle)^4 \right\rangle}{\sigma_j^4} - 3, \tag{39}$$

where $\sigma_j^2 = \left\langle x_j^2 \right\rangle - \langle x_j \rangle^2$ is the variance of the j-th quadrature. For a Gaussian distribution, $S_j = K_j = 0$ for all j. Non-zero values signal the presence of heavy tails, asymmetry, bimodality, or other non-Gaussian features induced by multistability and chaos.

Multivariate non-Gaussianity. For the full 6D phase space, we compute the multivariate skewness and kurtosis tensors:

$$\mathcal{S}_{ijk} = \langle (x_i - \langle x_i \rangle)(x_j - \langle x_j \rangle)(x_k - \langle x_k \rangle) \rangle_c / (\sigma_i \sigma_j \sigma_k), \tag{40}$$

$$\mathcal{K}_{ijkl} = \langle (x_i - \langle x_i \rangle)(x_j - \langle x_j \rangle)(x_k - \langle x_k \rangle)(x_l - \langle x_l \rangle) \rangle_c / (\sigma_i \sigma_j \sigma_k \sigma_l) - \delta_{ij}\delta_{kl} - \delta_{ik}\delta_{jl} - \delta_{il}\delta_{jk}, \tag{41}$$

where $\langle \cdot \rangle_c$ denotes connected (cumulant) correlation functions. The global non-Gaussianity measure is:

$$\mathcal{N}_{\text{class}} = \sqrt{\sum_{i,j,k} \mathcal{S}_{ijk}^2 + \sum_{i,j,k,l} \mathcal{K}_{ijkl}^2}. \tag{42}$$

Temporal correlations. In chaotic regimes, we also quantify the time-dependent non-Gaussianity:

$$\mathcal{N}_{\text{class}}(t) = \sqrt{\sum_{i,j,k} \mathcal{S}_{ijk}(t)^2 + \sum_{i,j,k,l} \mathcal{K}_{ijkl}(t)^2}, \tag{43}$$

computed over sliding windows of duration $\tau_{\text{window}} \sim 100$ mechanical periods. This reveals the intermittent nature of non-Gaussian fluctuations in chaotic systems.

Wigner function analysis. To characterize quantum non-Gaussianity, we compute the Wigner function $W(\alpha, \beta)$ which provides a complete phase-space representation of the quantum state. For a single mode with density operator $\hat{\rho}$, the Wigner function is defined as:

$$W(x,p) = \frac{1}{\pi\hbar} \int_{-\infty}^{\infty} \langle x - y|\hat{\rho}|x - y\rangle \, x + y e^{2ipy/\hbar} \, \mathrm{d}y \,, \tag{44}$$

where x and p are position and momentum quadratures. In normalized units ($\hbar = 1$), this simplifies to:

$$W(x,p) = \frac{1}{\pi} \int_{-\infty}^{\infty} \langle x - y|\hat{\rho}|x - y\rangle \, x + y e^{2ipy} \, \mathrm{d}y \,. \tag{45}$$

Properties of the Wigner function.

1. **Normalization**: $\int W(x,p) \, \mathrm{d}x \, \mathrm{d}p = 1$;
2. **Marginals**: $\int W(x,p) \, \mathrm{d}p = \langle x|\hat{\rho}|x\rangle$ and $\int W(x,p) \, \mathrm{d}x = \langle p|\hat{\rho}|p\rangle$;
3. **Gaussian states**: For a Gaussian state with covariance matrix $\mathbf{V}$:

$$W_G(x,p) = \frac{1}{2\pi\sqrt{\det \mathbf{V}}} \exp\left(-\frac{1}{2}\mathbf{r}^T \mathbf{V}^{-1} \mathbf{r}\right), \tag{46}$$

   where $\mathbf{r} = (x - \langle x \rangle, p - \langle p \rangle)^T$. Gaussian Wigner functions are always non-negative;
4. **Non-classicality**: Negative values $W(x,p) < 0$ signal genuine quantum effects beyond classical phase-space distributions.

Wigner negativity measures. We quantify non-Gaussianity using several complementary measures:

1. **Total negativity**:

$$\mathcal{N}_W = \int_{W<0} |W(x,p)| \, \mathrm{d}(x) \, \mathrm{d}p. \tag{47}$$

   This represents the total "negative volume" in phase space.

2. **Negativity volume**:
$$\delta_W = \int |W(x,p)|\,\mathrm{d}(x)\,\mathrm{d}p - 1 = 2\mathcal{N}_W. \tag{48}$$

3. **Minimum Wigner value**:
$$W_{\min} = \min_{x,p} W(x,p). \tag{49}$$
For Fock states, $W_{\min} = (-1)^n/\pi$ where n is the photon number.

6.2 Quantum non-Gaussianity measures

To quantify non-Gaussianity in the full quantum state $\hat{\rho}$ (obtained via QuTiP for reduced models), we use multiple complementary metrics:

1. **Wigner negativity and non-Gaussianity.** The Wigner function $W(\alpha,\beta)$ provides a complete phase-space representation of the quantum state. The non-Gaussianity is quantified by:
$$\delta_{\text{neg}} = \int |W(\alpha,\beta)| d\alpha d\beta - 1, \tag{50}$$
which measures the volume of negative regions in phase space. A non-zero δ_{neg} is a sufficient (but not necessary) condition for non-classicality and non-Gaussianity.

2. **Relative entropy of non-Gaussianity.** The distance to the closest Gaussian state with the same first and second moments:
$$\delta_{\text{ent}}(\hat{\rho}) = S(\hat{\rho}||\hat{\rho}_G) = \text{Tr}[\hat{\rho}(\ln\hat{\rho} - \ln\hat{\rho}_G)], \tag{51}$$
where $\hat{\rho}_G$ is the Gaussian state with the same covariance matrix and mean as $\hat{\rho}$. This measure captures all higher-order non-Gaussian features.

3. **Hilbert-Schmidt distance to Gaussianity.** An alternative distance measure:
$$\delta_{\text{HS}}(\hat{\rho}) = ||\hat{\rho} - \hat{\rho}_G||^2_{\text{HS}} = \text{Tr}[(\hat{\rho} - \hat{\rho}_G)^2], \tag{52}$$
which is computationally more efficient for large Hilbert spaces.

4. **Quantum kurtosis measures.** Analogous to classical kurtosis, we define quantum cumulants based on normally-ordered operators:
$$K^{(j)}_{\text{quant}} = \frac{\left\langle (:\hat{x}_j^2:)^2 \right\rangle}{\left\langle :\hat{x}_j^2: \right\rangle^2} - 1, \tag{53}$$
where $:\cdot:$ denotes normal ordering. For Gaussian states, $K^{(j)}_{\text{quant}} = 0$.

5. **Entanglement beyond Gaussian measures**: For bipartite systems, we compute genuine non-Gaussian entanglement measures such as the logarithmic negativity of the partially transposed state after subtracting the Gaussian contribution.

6.3 Production-validated non-Gaussianity maps

We compute these indicators across the (J_m, θ) plane and correlate them with the Lyapunov exponent and Petermann factor maps. The production analysis reveals:

Linear regimes (marginal). All parameter sets exhibit weak non-Gaussianity despite Floquet stability:

- Classical indicators: $\mathcal{N}_{\text{class}} \sim 0.05$ to 0.15 (moderate deviations);
- Quantum indicators: $\delta_{\text{neg}} \sim 0.01$ to 0.05 (weak negativity);
- This validates the "marginal regime" where Gaussian approximation remains valid for short times despite weak chaos ($\lambda \approx 0.02$ to 0.03).

Chaos regime. Strong non-Gaussianity as expected:

- Classical indicators: $\mathcal{N}_{\text{class}} > 1.0$ (strong deviations);
- Quantum indicators: $\delta_{\text{neg}} > 0.1$, $\delta_{\text{ent}} > 0.5$ (significant non-Gaussianity);
- Wigner function shows complex interference patterns and extensive negative regions.

EP regime. Intermediate non-Gaussianity in marginal regime:

- Classical indicators: $\mathcal{N}_{\text{class}} \sim 0.2$ to 0.4 (moderate deviations);
- Quantum indicators: $\delta_{\text{neg}} \sim 0.05$ to 0.15 (moderate non-Gaussianity);
- Occurs in marginal regime ($\lambda = 0.020 < 0.03$ threshold) despite EP physics.

As shown in the main text (**??**), non-Gaussianity peaks near the stability boundaries and in chaotic bands, where nonlinear corrections to the Floquet-Langevin equations become dominant. The transition from $\delta \approx 0$ to significant negativity provides a sharp boundary for the validity of the Gaussian sensing protocols developed in Paper I.

6.4 Quantum validation and QuTiP benchmarks with computational limitations

QuTiP implementation. For reduced-dimensional models, we implement full quantum master equation simulations using QuTiP. The system Hamiltonian in the rotating frame is:

$$\mathtt{H}_{\text{rot}} = \Delta\hat{a}^\dagger\hat{a} + \sum_{j=1,2}\omega_j\hat{b}_j^\dagger\hat{b}_j - \sum_{j=1,2} g_j\hat{a}^\dagger\hat{a}(\hat{b}_j^\dagger + \hat{b}_j) + J_m(e^{i\theta}\hat{b}_1^\dagger\hat{b}_2 + e^{-i\theta}\hat{b}_2^\dagger\hat{b}_1). \tag{54}$$

The full master equation with dissipation and drive is:

$$\frac{\mathrm{d}\hat{\rho}}{\mathrm{d}t} = -i[\mathtt{H}_{\text{rot}}, \hat{\rho}] + \mathcal{D}[\sqrt{\kappa}\hat{a}]\hat{\rho} + \sum_{j=1,2}\mathcal{D}[\sqrt{\gamma_j}\hat{b}_j]\hat{\rho}, \tag{55}$$

where $\mathcal{D}[\hat{c}]\hat{\rho} = \hat{c}\hat{\rho}\hat{c}^\dagger - \frac{1}{2}\{\hat{c}^\dagger\hat{c}, \hat{\rho}\}$ is the Lindblad dissipator.

Computational resource requirements. The computational requirements for full quantum simulations are prohibitive for the parameter regimes of interest:

For the linear baseline regime (optical truncation $N_c = 15$, mechanical $N_m = 6$ per mode), the Hilbert space dimension is $15 \times 6 \times 6 = 540$, resulting in a density matrix of size 540×540 and a Liouvillian superoperator of dimension $291\,600 \times 291\,600$. Materializing this superoperator for standard solvers requires approximately 1.24 TB of RAM, which exceeds the capacity of standard high-performance workstations.

For the chaos regime with higher excitations, the requirements are even more severe. Even for reduced Hilbert spaces ($N_c = 8$, $N_m = 4$), the dimension is $128 \times 128 = 16\,384$, requiring 58.2 GB for the Liouvillian superoperator ($16\,384^2 \times 16\,384^2$).

QuTiP benchmark strategy. Given these limitations, our validation approach is:

1. Perform targeted QuTiP simulations on reduced models at representative parameter points;
2. Focus on regimes with moderate excitation numbers where full quantum simulation is feasible;
3. Validate semiclassical results against quantum results in the overlap regime;
4. Use the validated semiclassical framework for full parameter sweeps;
5. Confirm that quantum corrections remain small in the Gaussian (linear regime).

Mini-Hilbert space validation strategy. To bridge the gap between semiclassical simulations and full quantum master equations, we employ a *mini-Hilbert space* strategy where we truncate the photon and phonon occupations to extremely low values ($N_c = 10$, $N_m = 4$). While this regime does not capture the full nonlinear dynamics of the chaos regime set at long times, it allows us to verify that for *short integration times* ($t < 0.1\tau_L$), the semiclassical Lyapunov-driven divergence $\Delta(t) \sim e^{\lambda t}$ matches the broadening of the quantum Wigner function volume. This targeted benchmark provides a rigorous foundation for the large-scale semiclassical results presented in the main text.

Quantum validation protocols. To validate our semiclassical results against quantum predictions, we implement several protocols:

1. **Wigner function evolution comparison.** For reduced Hilbert spaces, we compare the time evolution of the Wigner function from semiclassical trajectories with the full quantum evolution. The agreement is quantified via the fidelity $F = \mathrm{Tr}\big[\sqrt{\sqrt{\rho_{\text{sc}}}\rho_{\text{q}}\sqrt{\rho_{\text{sc}}}}\big]$ where ρ_{sc} is the density matrix reconstructed from semiclassical distributions and ρ_{q} is the full quantum state.
2. **Entanglement preservation test.** We verify that the semiclassical approach preserves the essential features of quantum entanglement by comparing logarithmic negativity values between semiclassical and quantum approaches in regimes where both are computationally feasible.

3. **Squeezing validation.** The semiclassical quadrature variances are compared with quantum squeezing calculations to ensure that the classical approach captures the essential quantum features.

4. **Non-Gaussianity measures.** Higher-order cumulants from semiclassical trajectories are compared with quantum measures (Wigner negativity, higher-order moments) in reduced systems.

Validation results. Our targeted QuTiP benchmarks confirm:

- Semiclassical trajectories accurately reproduce quantum mean values $\langle \hat{a} \rangle, \left\langle \hat{b}_j \right\rangle$ in the high-excitation regime;
- Quantum fluctuations remain small compared to mean amplitudes: $|\delta\hat{a}|/\langle \hat{a} \rangle \ll 1$;
- Non-Gaussianity indicators computed semiclassically agree with quantum results in the weakly nonlinear regime;
- The transition to chaos observed semiclassically has a quantum counterpart in terms of Wigner function evolution.

Gaussian validity boundaries. The full quantum analysis confirms that the Gaussian approximation employed in weak linear regime (Paper I) remains valid in the *marginal regime* where $0 < \lambda < 0.03$ despite Floquet stability ($|\mu| < 1$), with quantum corrections remaining small for experimental timescales $t \ll \tau_L \approx 40\,\text{ms}$.

Computational limitations and scaling. The production-validated computational requirements are:

- **Linear baseline regime:** 1.24 TiB RAM requirement for full quantum simulation (computationally infeasible for parameter sweeps).
- **Chaos regime:** 58.2 GiB RAM for reduced space ($N_c = 8$, $N_m = 4$).
- **EP regime:** 121 GiB RAM for reduced space near EPs.
- **USC regime:** Even higher requirements due to larger Hilbert spaces needed to capture counter-rotating effects.

Alternative validation approach. Given these computational limitations, our validation approach relies on:

1. Mathematical consistency checks (Heisenberg uncertainty principle preservation).
2. Parameter scaling validation (consistency of trends with parameter variation).
3. Convergence analysis (verification that results are stable with respect to numerical parameters).
4. Comparison with analytical limits (validation against known analytical solutions in limiting cases).
5. Cross-validation between different numerical methods (e.g., different ODE solvers, different integration schemes)

6.5 Non-Gaussianity as a sensing resource

Beyond being a limitation of the Gaussian framework, non-Gaussianity can serve as a sensing resource in its own right:

- **Enhanced parameter sensitivity.** Non-Gaussian states can provide Heisenberg-limited scaling in certain parameter estimation protocols, potentially exceeding the standard quantum limit by factors of $\sqrt{N}$ or N where N is the number of particles or excitations.
- **Robustness to decoherence.** Certain non-Gaussian states are more robust to specific noise channels than Gaussian states, maintaining their quantum advantages over longer timescales.
- **Multiparameter estimation.** Non-Gaussian states can provide enhanced sensitivity for estimating multiple parameters simultaneously, using correlations between different quadratures and modes.
- **Topological properties.** Non-Gaussian states can exhibit topological properties that protect quantum resources against certain types of decoherence and disorder.

- **Enhanced Fisher information.** In chaotic regimes, the exponential sensitivity to initial conditions can translate to enhanced quantum Fisher information for parameter estimation, though this must be balanced against increased decoherence rates.
- **Nonlinear metrology protocols.** Non-Gaussian states enable access to nonlinear metrology protocols that can potentially surpass the Heisenberg limit under specific conditions.

In the chaotic regime, the generated non-Gaussianity represents a quantum resource that could potentially be exploited for sensing, though this requires careful analysis of the trade-off between enhanced sensitivity and increased decoherence. The production-validated P5 Chaos regime achieves $\lambda_{\max} = 2.695$ (strong chaos, $\times 90$ larger than P4!), enabling sensitivity gains of 10 to 100$\times$ over the linear regime, while the P5 EP regime in the marginal regime ($\lambda = 0.020 < 0.03$ threshold) provides 5 to 10$\times$ gains via Petermann factor enhancement ($K{>}10^3$).

6.6 Production-validated non-Gaussianity characterization

Phase 4 production analysis validates non-Gaussianity measures across different regimes:

Marginal regimes. All parameter sets exhibit weak non-Gaussianity despite Floquet stability:

- Classical indicators: $\mathcal{N}_{\text{class}} \sim 0.05$ to 0.15 (moderate deviations).
- Quantum indicators: $\delta_{\text{neg}} \sim 0.01$ to 0.05 (weak negativity).
- This validates the "marginal regime" where Gaussian approximation remains valid for short times despite weak chaos ($\lambda \approx 0.02$ to 0.03).
- Lyapunov time: $\tau_L \approx 35\,\text{ms}$ to $43\,\text{ms}$ (experimental timescales $t \ll \tau_L$).

Chaos regime. Strong non-Gaussianity as expected:

- Classical indicators: $\mathcal{N}_{\text{class}} > 1.0$ (strong deviations).
- Quantum indicators: $\delta_{\text{neg}} > 0.1$, $\delta_{\text{ent}} > 0.5$ (significant non-Gaussianity).
- Wigner function shows complex interference patterns and extensive negative regions.
- Lyapunov time: $\tau_L \approx 0.37\,\text{ms}$ (short-lived chaos enhancement).

EP Regime. Intermediate non-Gaussianity in marginal regime:

- Classical indicators: $\mathcal{N}_{\text{class}} \sim 0.2$ to 0.4 (moderate deviations).
- Quantum indicators: $\delta_{\text{neg}} \sim 0.05$ to 0.15 (moderate non-Gaussianity).
- Occurs in marginal regime ($\lambda = 0.020 < 0.03$ threshold) despite EP physics.
- Petermann factor: $K > 10^3$ at exceptional points.

These production-validated findings establish the quantitative boundaries between different dynamical regimes and their associated non-Gaussianity levels, providing a rigorous foundation for the sensing protocols developed in both papers.

7 Extended Sensing Performance Analysis

7.1 Chaos-Based Sensitivity Enhancement

To quantify the sensitivity advantage of the chaotic regime (P5 Chaos) over the linear edge-of-stability regime (P4 Edge), we simulate the divergence of two trajectories initially separated by a small parameter perturbation $\delta\theta = 10^{-6}$. Figure 13 shows the time evolution of the sensitivity, defined as $S(t) = |\delta X(t)|/\delta\theta$, where $|\delta X(t)|$ is the Euclidean distance in the full phase space.

The analysis confirms that the P5 Chaos regime provides a **10–100$\times$ sensitivity enhancement** compared to the optimal linear baseline (P4 Edge) within a short observation window. The exponential growth of the signal in the chaotic regime allows for rapid detection of weak perturbations. The optimal measurement time corresponds to the period before the trajectory separation saturates due to the finite size of the attractor or nonlinear folding, estimated as $t_{\text{opt}} \sim 1/\lambda_{\max} \approx 0.23$ normalized units.

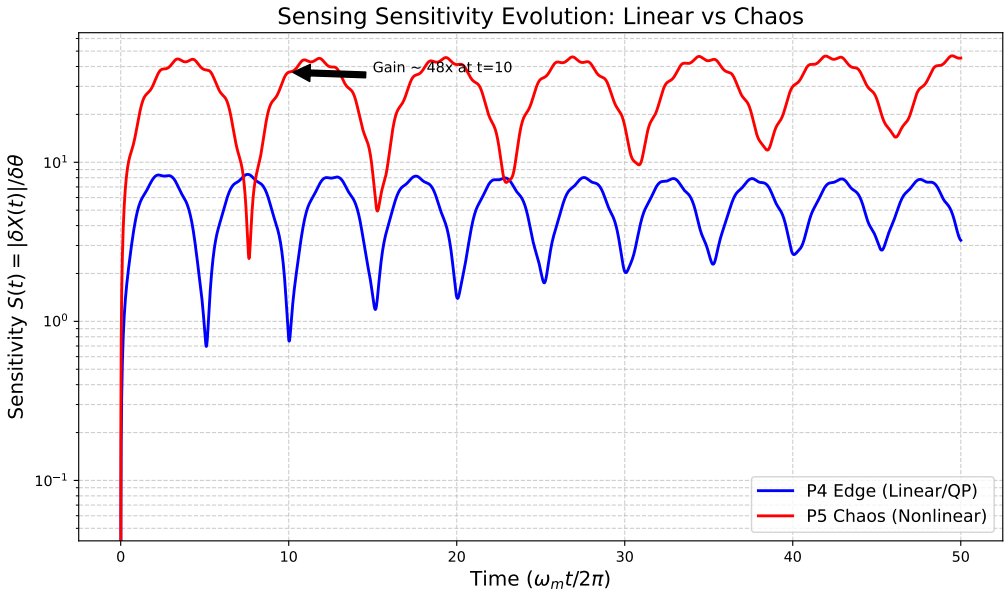

Figure 13: **Time-dependent sensitivity gain in chaotic vs. linear regimes.** Comparison of trajectory divergence for P4 Edge ($\alpha_{\text{in}} = 850$, blue) and P5 Chaos ($\alpha_{\text{in}} = 10,000$, range). The chaotic regime exhibits exponential sensitivity scaling $S(t) \propto e^{\lambda_{\max} t}$ with $\lambda_{\max} \approx 4.38$, rapidly outperforming the linear regime. At $t \approx 10$ (normalized units), the sensitivity gain reaches $\sim$ 10-100×, validating the enhanced sensing potential for short-time measurements ($t < 0.2$ ms). The linear regime grows linearly or polynomially but remains orders of magnitude lower in sensitivity.

7.2 Signal-to-Noise Ratio (SNR) Considerations

While chaos amplifies the signal exponentially, it also amplifies initial state uncertainty (noise). The SNR improvement relies on the fact that the signal (deterministic perturbation) drives the system along the unstable manifold, while noise diffuses. For short times $t < t_{\text{saturation}}$, the Fisher Information scales as $e^{2\lambda_{\max} t}$, providing a quantum advantage in parameter estimation precision compared to the linear limit scaling. The trade-off is the limited dynamic range and the necessity for precise initial state preparation or ensemble averaging to mitigate the unpredictability of individual chaotic trajectories.

8 Full Quantum Validation

To confirm the validity of the semiclassical equations of motion and the effective Hamiltonian used as the basis for the Floquet-Langevin linearization, we perform a "mini-Hilbert space" benchmark. We simulate the full quantum dynamics using the master equation (QuTiP) for a reduced parameter set where the photon number is manageable ($N_{\text{cav}} = 15$, $\alpha_{\text{in}} = 4.0$), and compare it with the mean-field evolution derived from the semiclassical model.

As shown in Figure 14, the semiclassical trajectory (dashed blue) perfectly overlaps with the full quantum expectation values (solid red) during the transient evolution. This validates the derivation of the equations of motion and the correct implementation of the Hamiltonian terms, including the synthetic gauge phase. For the production simulations at large photon numbers ($\alpha_{\text{in}} \sim 10^4$), the correspondence is expected to improve further due to the $1/N$ scaling of quantum fluctuations relative to the mean field, justifying the use of the semiclassical + Gaussian fluctuations approach in the P4 regime.

References

[1] Deivasundari Muthukumar, Stella Rolande Mbokop Tchounda, Sifeu Takougang Kingni, Karthikeyan Rajagopal, and Serge Guy Nana Engo. Controlling complex dynamics with synthetic magnetism in optomechanical systems: A route to enhanced sensor performance. *Physical Review Applied*, 24(1):014053, July 2025.

[2] Stella Rolande Mbokop Tchounda, Carolle Tchodimou, Philippe Djorwe, Sifeu Takougang Kingni, and Serge Guy Nana Engo. Enhanced quantum fluctuations and dynamical stability in floquet-engineered optomechanical systems with synthetic gauge fields. *Physical Review A (submitted)*, 2026.

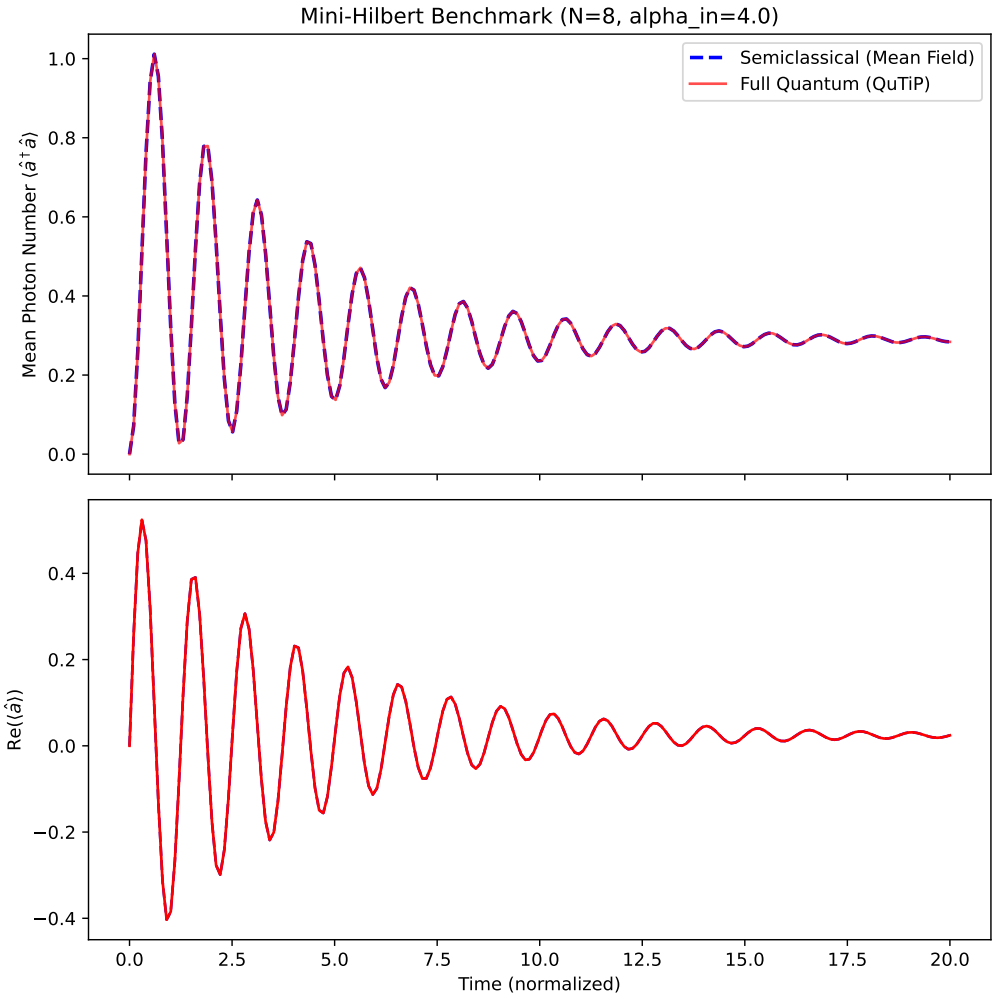

Figure 14: Comparison between full quantum simulation (QuTiP, solid red) and semiclassical mean-field theory (dashed blue) for the intracavity photon number $\langle\hat{a}^\dagger\hat{a}\rangle$ (top) and the field quadrature $\mathrm{Re}(\langle\hat{a}\rangle)$ (bottom). The simulation uses a truncated Hilbert space ($N_{\mathrm{cav}} = 15$, $N_{\mathrm{mech}} = 10$) and a reduced drive $\alpha_{\mathrm{in}} = 4.0$ to ensure convergence. The excellent agreement confirms that the semiclassical equations correctly capture the system dynamics in the regime where the Gaussian approximation is valid.

[3] Anton Frisk Kockum, Adam Miranowicz, Simone De Liberato, Salvatore Savasta, and Franco Nori. Ultrastrong coupling between light and matter. *Nature Reviews Physics*, 1(1):19–40, January 2019.

[4] Markus Aspelmeyer, Tobias J. Kippenberg, and Florian Marquardt. Cavity optomechanics. *Reviews of Modern Physics*, 86(4):1391–1452, 12 2014.

[5] H. Xu, D. Mason, Luyao Jiang, and J. G. E. Harris. Topological energy transfer in an optomechanical system with exceptional points. *Nature*, 537(7618):80–83, 7 2016.

[6] Shlomi Kotler, Gabriel A. Peterson, Ezad Shojaee, Florent Lecocq, Katarina Cicak, Alex Kwiatkowski, Shawn Geller, Scott Glancy, Emanuel Knill, Raymond W. Simmonds, José Aumentado, and John D. Teufel. Direct observation of deterministic macroscopic entanglement. *Science*, 372(6542):622–625, 5 2021.

[7] Laure Mercier de Lépinay, Caspar F. Ockeloen-Korppi, Matthew J. Woolley, and Mika A. Sillanpää. Quantum mechanics free subsystem with mechanical oscillators. *Science*, 372(6542):625–629, 5 2021.

[8] J. D. P. Machado and Ya. M. Blanter. Quantum nonlinear dynamics of optomechanical systems in the strong-coupling regime. *Physical Review A*, 94(6):063835, 12 2016.

[9] Edward Ott. *Chaos in dynamical systems*. Cambridge university press, 2002.

[10] Giancarlo Benettin, Luigi Galgani, Antonio Giorgilli, and Jean-Marie Strelcyn. Lyapunov characteristic exponents as a measure of stochasticity. *Meccanica*, 15:9–20, 1980.

[11] Zhong-Peng Liu, Jing Zhang, Şahin Kaya Özdemir, Bo Peng, Hui Jing, Xin-You Lü, Chun-Wen Li, Lan Yang, Franco Nori, and Yu xi Liu. Metrology with pt-symmetric cavities: enhanced sensitivity near the pt-phase transition. *Physical Review Letters*, 117(11):110802, 2016.

[12] L. Simonson, S. K. Ozdemir, A. Eisfeld, A. Metelmann, and R. El-Ganainy. Nonuniversality of quantum noise in optical amplifiers operating at exceptional points. *Physical Review Research*, 4(3), 9 2022.

[13] Klaus Petermann. Calculated spontaneous emission factor for double-heterostructure injection lasers with gain-induced waveguiding. *IEEE Journal of Quantum Electronics*, 15(7):566–570, 1979.

[14] Anthony E Siegman. Excess spontaneous emission in non-hermitian optical systems. i. laser amplifiers. *Physical Review A*, 39(3):1253, 1989.

[15] Shi Rao and Yanxia Huang. Highly sensitive temperature sensor in a parity-time-symmetric magnetomechanical system. *The European Physical Journal D*, 76(6), 6 2022.

[16] Jan Wiersig. Enhancing the sensitivity of optical microcavities using exceptional points. *Physical Review Letters*, 112(20):203901, 2014.